Large Nernst effect and possible temperature-induced Lifshitz transition in topological semimetal $YbMnSb_2$

Sheng Xu,[1] Chenxi Jiang,[1,2] Shu-Xiang Li,[1,2] Jun-Jian Mi,[1,2] Zheng Li,[1,2] Tian-Long Xia,[3] Qian Tao,[1,2] and Zhu-An Xu[1,2,4,*]

[1]*Zhejiang Province Key Laboratory of Quantum Technology and Device, School of Physics, Zhejiang University, Hangzhou 310027, China*
[2]*State Key Laboratory of Silicon and Advanced Semiconductor Materials, Zhejiang University, Hangzhou 310027, China*
[3]*Department of Physics and Beijing Key Laboratory of Opto-electronic Functional Materials & Micro-nano Devices, Renmin University of China, Beijing 100872, China*
[4]*Hefei National Laboratory, Hefei 230088, China*

(Received 30 January 2023; revised 29 May 2023; accepted 5 June 2023; published 27 June 2023)

Topological materials provide an interesting platform in the study of thermoelectric effect due to their novel electronic properties. Here we report the magneto-Seebeck (MS) effect, large Nernst effect, and a possible temperature-induced Lifshitz transition in topological semimetal $YbMnSb_2$. It exhibits evident quantum oscillations in the MS effect from which six frequencies are extracted and a light effective mass of F_4 is obtained. The large Nernst effect with the Nernst thermopower of about 40 μVK^{-1} is discovered around 120 K and 14 T. Combining the analysis of the first-principles calculations and the Hall effect, we suggest that the large Nernst signal could mainly stem from the Dirac bands-induced high mobility and small Fermi energy (ε_F). Besides, it could be further enhanced by the modified carrier properties resulting from the temperature-induced Lifshitz transition through the so-called ambipolar effect.

DOI: 10.1103/PhysRevB.107.245138

I. INTRODUCTION

In the past decades, searching for new topological states and studying their novel physical properties have become the hot topics in condensed-matter physics and material science [1–4]. Among them, many topological materials are demonstrated to host excellent thermoelectric properties, which have great value in application in thermoelectric generation and heat flow sensors [5–9]. In recent years, more attention has been focused on materials with better thermoelectric properties especially with the large Nernst effect [10–13]. To improve the Nernst signal, many approaches have been reported. First, the Nernst signal could be enhanced in a multiband system, which is known as the ambipolar effect. $NbSe_2$ is one of the typical materials displaying the ambipolar effect [14]. Second, the Nernst signal could be enhanced in a system with high mobility and small Fermi energy (ε_F) [11]. Third, the giant anomalous Nernst effect could be observed in topological materials, which is believed to be induced by the intrinsic Berry curvature [12,15–22]. Linearly dispersive band crossing is a typical characteristic of topological materials. When the band crossing is near the E_F (small ε_F), the Dirac/Weyl fermion participates in the transport directly, leading to many novel properties, such as ultrahigh mobility and nontrivial Berry phase. Benefited from the high mobility and the small ε_F, topological materials are reasonably expected to have excellent transverse thermoelectric properties. In addition, the Dirac semimetal Cd_3As_2 [15,16], the Weyl semimetal TaAs, TaP [12,17], the magnetic Weyl semimetals, such as Mn_3Sn [18], $Co_3Sn_2S_2$ [19,20], Co_2MnGa [21], and the nodal-line semimetal MnAlGe [22] were also reported to host a giant intrinsic anomalous Nernst effect.

On the other hand, the Lifshitz transition is a quantum phase transition where the Fermi surface changes abruptly and could be driven by the magnetic field, doping, and high pressure [23–26]. Such remarkable changes in the Fermi surface could result in a giant contribution to thermoelectric effects, including the Nernst effect. Nowadays, the temperature-induced Lifshitz transition has been studied in many materials [27–30] in which the chemical potential shifts with increasing temperature and the Fermi surface changes correspondingly. Owing to the band crossing near Fermi level in topological semimetals, their carrier concentration and mobility could be greatly affected by temperature, which would lead to the easy occurrence of a temperature-dependent Lifshitz transition and the ambipolar effect-induced large Nernst signal [15,17]. However, the study of temperature-induced Lifshitz transition is still rare.

In $YbMnSb_2$, different experimental results show different topological states [31–34]. However, Soh *et al.* determined the *C*-type antiferromagnetism (AFM) in $YbMnSb_2$ with the moments of Mn lying along the *c* axis by performing unpolarized and polarized single-crystal neutron diffractions, indicating the existence of the gapped Dirac node [34]. In this paper, we performed detailed longitudinal and transverse thermoelectric measurements at various temperatures on $YbMnSb_2$. The magneto-Seebeck (MS) effect displays evident quantum oscillations with several frequencies. The effective mass of

*zhuan@zju.edu.cn

the main frequency F_4 (68.5 T) is extracted to be $0.07m_e$ after fitting by the thermal damping factor in the Lifshitz-Kosevich (LK) formula. With increasing temperature, the Nernst signal first increases below 120 K and reaches a maximum of about 40 μVK^{-1} ($B = 14$ T). Combining the analysis of the first-principles calculations and the Hall effect, the large Nernst effect in $YbMnSb_2$ is suggested to mainly stem from the Dirac bands-induced high mobility and small ε_F. Besides, a possible temperature-induced Lifshitz transition is also revealed by the electric, thermoelectric measurements, and the first-principles calculations. Consequently, the carrier properties are modified, leading to a further enhancement of the Nernst signal due to the so-called ambipolar effect.

II. EXPERIMENTAL AND CALCULATION DETAILS

Platelike $YbMnSb_2$ single crystals were grown by the self-flux method as described in Ref. [31]. The atomic composition of the obtained single crystal was measured to be about Yb: Mn: Sb = 1: 1: 2 by energy dispersive x-ray spectroscopy. Powder x-ray diffraction (XRD) patterns were collected from the PANalytical x-ray diffractometer (Empyrean) with monochromatic Cu α_1 radiation. The (001) plane was determined by XRD patterns on a single crystal. The measurements of transport properties were performed on the Quantum Design physical property measurement system. The longitudinal and transverse resistances were collected by the standard four-probe method. The thermal gradient was established by a 1-kΩ resistor heater in the measurements of thermoelectric properties. The Nernst and Hall signals were obtained from the difference of the results in positive and negative fields in order to effectively remove the longitudinal contribution from the voltage probe misalignment.

The first-principles calculations of the electronic structure of bulk $YbMnSb_2$ were performed by using the Vienna *ab initio* simulation package, with the generalized gradient approximation in the Perdew-Burke-Ernzerhof type as the exchange-correlation energy. The cutoff energy was set to 400 eV and Γ-centered $16 \times 16 \times 10$ k mesh were sampled over the Brillouin zone integration. The experimental lattice constants $a = 4.37$, $c = 11.01$ Å were used for all the calculations. The tight-binding model of $YbMnSb_2$ was constructed by the WANNIER90 with $3d$ orbitals of Mn and $5p$ orbitals of Sb, which is based on the maximally localized Wannier functions [35].

III. RESULTS AND DISCUSSIONS

Figure 1(a) exhibits the in-plane Seebeck coefficient S_{xx} in a temperature range from 2.5 to 300 K. The Seebeck coefficient is about 148 $\mu V\,K^{-1}$ at 300 K, which is comparable with that reported by Pan *et al.* [36]. Figure 1(b) presents the Seebeck coefficient versus magnetic field (MS effect) at various temperatures with the $B \parallel c$ configuration. The Seebeck coefficient S_{xx} increases with increasing field and exhibits obvious quantum oscillations. After subtracting the smooth background, the oscillatory components of S_{xx} at different temperatures are plotted in Fig. 1(c). Different to the Shubnikov–de Haas (SdH) oscillations and the de Haas–van Alphen (dHvA) oscillations where the oscillatory amplitudes would increase to maximum as $T \to 0$, the oscillatory amplitudes of S_{xx} first increase with decreasing temperature and reach a maximum around 8 K, then decrease and vanish as temperature is close to 0 K. Such a vanishing Seebeck effect at low temperature is due to the vanishing entropy of charge carriers when $T \to 0$. After employing the fast Fourier transform (FFT) analysis as shown in Fig. 1(d), several frequencies with the most apparent one being F_4 (68.3 T) are extracted. The FFT patterns are consistent with the results of the SdH oscillations and the dHvA oscillations [31]. However, there are additional frequencies besides F_4, indicating that $YbMnSb_2$ is a multiband system and the MS quantum oscillations could reflect more details of the Fermi-surface structure. According to the Onsager relation $F = (\hbar/2\pi e)A_F$, frequency F is proportional to the extreme cross-section A_F of the Fermi-surface normal to the magnetic field. The extreme cross-section area of F_4 is estimated to be 6.52×10^{-3} Å^{-2}, which is only 0.3% of the total area of the first Brillouin zone. The details of the frequencies are listed in Table I.

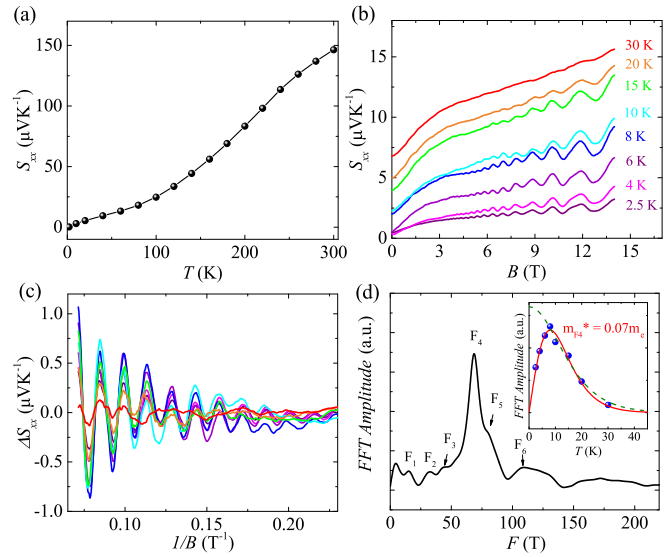

FIG. 1. (a) Temperature-dependent Seebeck coefficient. (b) Magneto-Seebeck effect at low temperature with $B \parallel c$ configuration. (c) Oscillatory component ΔS_{xx} plotted as a function of $1/B$ after subtracting a smooth background. (d) FFT spectra of ΔS_{xx} at 6 K. The inset is the effective mass fitted by the thermal damping factor.

TABLE I. The parameters extracted from MS oscillations in $YbMnSb_2$ with the $B \parallel c$ configuration. F is the frequency; m^*/m_e is the ratio of the effective mass to the electron mass; A_F is the extreme cross section of the Fermi surface; and k_F is the Fermi vector.

	F_1	F_2	F_3	F_4	F_5	F_6
$F(T)$	14.8	31.9	44.1	68.5	79.5	108.7
m^*/m_e				0.07		
$A_F 10^{-3}$ (Å^{-2})	1.41	3.05	4.21	6.52	7.59	10.38
$k_F 10^{-2}$ (Å^{-1})	2.12	3.11	3.66	4.56	4.92	5.75

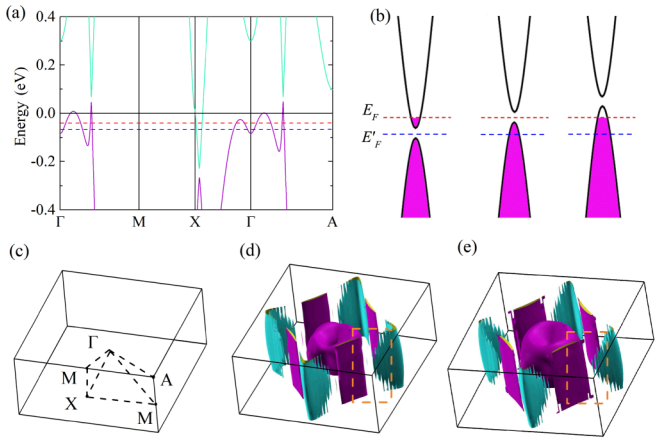

FIG. 2. (a) The band structure of $YbMnSb_2$ with SOC. The red and blue dashed lines represent the chemical potential shift −50 and −80 meV from the Fermi level, respectively. (b) Schematic of the evolution of the gapped nodal line with chemical potential at low temperature (red dashed line) and high temperature (blue dashed line). (c) High-symmetry point in the first Brillouin zone. (d) and (e) Fermi surfaces with a shift of approximately −50 and −80 meV from the Fermi level, respectively.

In SdH and dHvA oscillations, the thermal damping factor in the LK formula is

$$R_T = \frac{\alpha PX}{\sinh(\alpha PX)}, \tag{1}$$

where $\alpha = 2\pi^2 k_B/e\hbar$, $X = m^*T/B$, and P is the number of the harmonics [37]. According to the previous works, the thermal damping factor of the magnetothermopower oscillations in the LK formula should be described as [38–42],

$$R_T = \frac{(\alpha PX)\coth(\alpha PX) - 1}{\sinh(\alpha PX)}. \tag{2}$$

Here, the oscillatory amplitude would reach a maximum at $\alpha P m^* T/B = 1.62$ [43]. The effective mass of F_4 is fitted to be $0.07m_e$ as shown by the red curve in the inset of Fig. 1(d). We also fit the temperature-dependent oscillatory amplitude above 8 K with Eq. (1) as shown by the olive dashed curve in the inset of Fig. 1(d), and the fitted effective mass is $0.05m_e$. The light effective mass probably stems from the Dirac band with linear dispersion, which is the typical characteristic of topological semimetals. The amplitudes of the rest frequencies are relatively small and, thus, it is hard to extract the effective masses.

The band structure with the spin-orbit coupling (SOC) effect is shown in Fig. 2(a). The calculations elucidate that a nodal line exists in the Γ-X-M plane when SOC is not considered, which is consistent with the previous reports [33]. Along this nodal line, the band crossing along Γ-M locates above Fermi level (E_F), resulting in a holelike Fermi surface, whereas the band crossing along Γ-X locates below E_F, leading to an electronlike Fermi surface. The simplified dispersion map along this line node is displayed in Supplemental Material Fig. S2 [44]. As we can see, the Dirac point locates exactly at E_F in the dispersion map cut at k_{ii} [Fig. S2(e) in the Supplemental Material [44]], which is known as an ideal Dirac point. When the SOC effect is included, the nodal line opens a small gap, and its evolution with E_F is displayed in Fig. 2(b). The E_F locates in the gap, the middle panel in Fig. 2(b), which is the ideal Dirac point when SOC is not included. The Dirac-like dispersion in $YbMnSb_2$ has already been observed by angle-resolved photoemission measurements [32]. In real materials, the E_F could be affected by many factors, such as vacancy, internal strain, or substitutions. It was reported that the E_F should shift about −75 meV from the calculations [32]. Because of the different sample synthesis method, a shift of −50 meV is selected in our case and the Fermi-surface structure in the first Brillouin zone is displayed in Fig. 2(d) where the Fermi surface changes from a holelike Fermi surface to an electronlike Fermi surface along the gapped nodal line. Besides, many small extreme cross sections exist at the comb-shaped electronlike Fermi surface on the *ab* plane, which is consistent with the multiple small frequencies in the quantum oscillations in the MS effect. The chemical potential shifts with increasing temperature towards the energy that has the minimum density of states according to the charge-neutrality condition. Because of the small ε_F, illustrated in Figs. 2(a) and 2(b), the Fermi-surface structure of $YbMnSb_2$ could be easily affected by the temperature-dependent shift of chemical potential. With increasing temperature, the chemical potential shifts deeper towards the valance band in $ZrTe_5$ but higher towards the conduction band in WTe_2 [28,29], respectively. In $YbMnSb_2$, it likely shifts deeper towards the valance band based on the Hall measurements as discussed below. The red and blue dashed lines in Figs. 2(a) and 2(b) display the chemical potential at low and high temperatures, respectively. As we can see, with increasing temperature, the chemical potential could shift from the conduction band to the gap [left panel in Fig. 2(b)] or from the gap to the valance band [middle panel in Fig. 2(b)] leading to the evolution of the electronic structures. For more clarity, the Fermi-surface structure with a shift of −80 meV from the Fermi level is exhibited in Fig. 2(e). In addition to the changes in the size of the Fermi surface, an extra branch of the holelike Fermi surface is generated along the gapped nodal line as illustrated in the orange dotted boxes in Figs. 2(d) and 2(e). Different from the usual temperature-induced Lifshitz transition where the Fermi surface could change abruptly at a specific temperature point, the temperature-induced Lifshitz transition in $YbMnSb_2$ may occur in a certain temperature range since $YbMnSb_2$ is a multiband system, and each pocket has a different ε_F. Besides, the temperature-induced Lifshitz transition in $YbMnSb_2$ should be more moderate because the temperature-induced Fermi surface change is relatively small in the existence of the trivial pockets around Γ. We tried to reveal this temperature-induced Lifshitz transition by measuring the quantum oscillations in the MS effect. However, the quantum oscillations only exist at relatively low temperatures far below the temperature of the Lifshitz transition in this material.

In order to further study the temperature-induced Lifshitz transition in this system, we applied detailed in-plane resistivity and Hall measurements. Figure 3(a) exhibits the temperature dependence of longitudinal resistivity. The inset is the derivative of resistivity with respect to temperature and shows a hump around 60 K, which is quite different from the behavior in conventional metal where the carrier transport

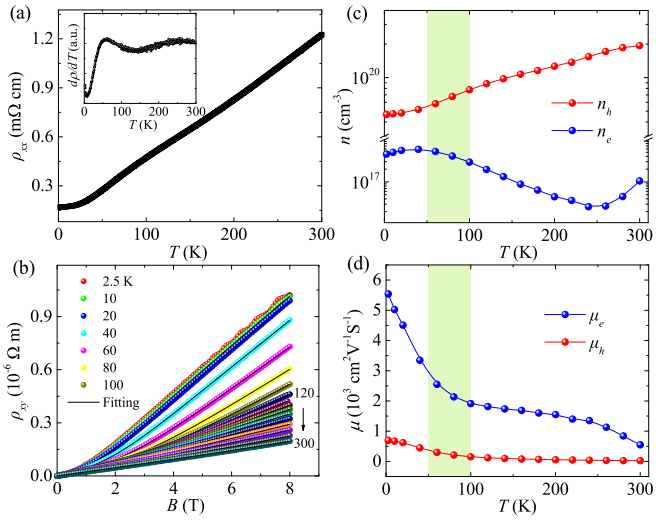

FIG. 3. (a) Temperature dependence of in-plane resistivity. The inset is the derivative of resistivity with respect to temperature. (b) Field dependence of the Hall resistivity at various temperatures. (c) and (d) Temperature dependence of carrier densities and mobility extracted from the two-band model fitting, respectively.

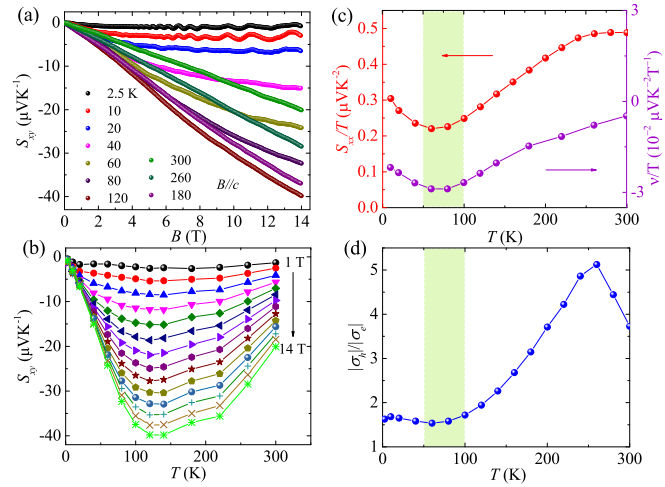

FIG. 4. (a) Field-dependent Nernst signal at different temperatures. (b) Temperature-dependent Nernst signal at different fields. (c) Temperature-dependent thermopower divided by temperature (S_{xx}/T) at zero field and Nernst coefficient divided by temperature (v/T) at 14 T. (d) Ratio of two-type charge-carrier conductivity ($|\sigma^h_{xy}|/|\sigma^e_{xy}|$).

should be mainly affected by scattering of phonons at relatively high temperatures. Figure 3(b) displays the isothermal field-dependent Hall resistivity from 2.5 to 300 K with the $B \parallel c$ configuration. The nonlinear temperature dependence of Hall resistivity indicates a multiband system. Besides, the Hall resistivity decreases faster around 60 K in the measured temperature range. The two-band model is used to fit the Hall resistivity,

$$\rho_{xy} = \frac{B}{e}\frac{\left(n_h\mu_h^2 - n_e\mu_e^2\right) + (n_h - n_e)(\mu_h\mu_e)^2B^2}{(n_h\mu_h + n_e\mu_e)^2 + (n_h - n_e)^2(\mu_h\mu_e)^2B^2}, \qquad (3)$$

where $n_{e,h}$ and $\mu_{e,h}$ represent the carrier density and mobility of the electron and hole, respectively. B is the magnetic field. The black line in Fig. 3(b) is the fitting result obtained by Eq. (3). The extracted carrier density and mobility are exhibited in Figs. 3(c) and 3(d), respectively. At 2.5 K, the density of the hole is about $n_h = 4.7 \times 10^{19}$ cm^{-3}, which is two orders of magnitude larger than the density of the electron, $n_e = 4.5 \times 10^{17}$ cm^{-3}. These results are consistent with the previous reports [31,32]. n_h increases with increasing temperature, and n_e exhibits the opposite temperature dependence, which indicates that the chemical potential shifts deeper towards the valance band with increasing temperature. The mobility of electron and hole is relatively high with the order of $u_e \sim 10^3$ and $u_h \sim 10^2$ cm^2 V^{-1} s^{-1}, respectively. For more details, the temperature-dependent density of electron-type carrier first increases with the increasing temperature and decreases above 60 K, whereas the hole-type carrier first increases slowly with the increasing temperature and increases faster above 60 K, indicating a possible temperature-induced Lifshitz transition. However, neither the density of electron-type nor hole-type carriers exhibits an abrupt change. These phenomena suggest that the temperature-induced Lifshitz transition in $YbMnSb_2$ is moderate and consistent with the discussion above. In addition, there is also an anomaly in the temperature-dependent carrier density and mobility of electron around 250 K, which could probably be another temperature-induced Lifshitz transition since the chemical potential shifts with increasing temperature and each pocket in the multiband $YbMnSb_2$ has a different ε_F.

Figure 4(a) displays the field-dependent Nernst effect at different temperatures, which increases with increasing field in the temperature range from 2.5 to 300 K and reaches a maximum of about 40 μV K^{-1} around 120 K and 14 T. Obvious quantum oscillations are also observed in the Nernst signal and the extracted frequencies are consistent with the MS effect. In order to get a better insight into the Nernst effect, we plot the temperature-dependent Nernst signal at different fields in Fig. 4(b). Under a specific field, there is a steady increase in $|S_{xy}|$ at low temperatures and then a gradual decrease as $T > 120$ K. The Nernst coefficient $v = S_{xy}/B$ at 14 T is about 3 μV K^{-1} T^{-1} around 120 K. In the zero-field limit, it attains the maximum 2.58 μV K^{-1} T^{-1}, which is much larger than the kagome semimetal CsV_3Sb_5 (~0.09 μV K^{-1} T^{-1}) [45], the superconductor $NbSe_2$ (~ − 0.12 μV K^{-1} T^{-1}) [14], the heavy fermion compound $CeCoIn_5$ (~ − 0.95 μV K^{-1}T^{-1}) [46] and is comparable to the cuprate superconductor $Ba_2Sr_{1.5}La_{0.5}CuO_6$ (~4.5μV K^{-1} T^{-1}) [47].

Next, let us discuss the possible origin of the large Nernst coefficient in $YbMnSb_2$. First, the large Nernst effect in $YbMnSb_2$ could stem from the ambipolar effect. In a two-band model, the Nernst signal could reach a maximum when $\sigma^h_{xy} = -\sigma^e_{xy}$, which is known as the ambipolar effect, as reported in CsV_3Sb_5 and $NbSe_2$ [11,14,45,48]. Fig. 4(d) presents the ratio of two-type charge carrier conductivity ($|\sigma^h_{xy}|/|\sigma^e_{xy}|$), which is calculated from the fitting results of Hall measurements ($\sigma = ne\mu$). As we can see, $|\sigma^h_{xy}|/|\sigma^e_{xy}|$ is almost unchanged with the value around 1.6 below 120 K and increases rapidly above 120 K. These characteristics indicate that the Nernst signal could be enhanced below 120 K through

the so-called ambipolar effect. Furthermore, the maximum of the Nernst signal should come around 60 K where the value of $|\sigma_{xy}^h|/|\sigma_{xy}^e|$ is closest to 1. However, the largest Nernst signal in $YbMnSb_2$ comes around 120 K, which indicates that there could be other mechanisms leading to the large Nernst effect in $YbMnSb_2$. In addition, the Nernst coefficients in CsV_3Sb_5 ($\sim 0.09\ \mu V\,K^{-1}\,T^{-1}$) [45,48] and $NbSe_2$ ($\sim -0.12\ \mu V\,K^{-1}\,T^{-1}$) [11,14] caused by the ambipolar effect are much smaller than that in $YbMnSb_2$ ($\sim 3\ \mu V\,K^{-1}\,T^{-1}$). Second, the large anomalous Nernst signal could be induced by the nonzero Berry curvature in topological materials [18–21]. Its family material $YbMnBi_2$ was reported to exhibit a giant anomalous Nernst signal due to the nonzero Berry curvature associated with the canted Mn moments [49,50]. However, $YbMnSb_2$ is a gapped nodal-line semimetal with the C-type collinear AFM when SOC is included, and its crystal structure possesses an inversion center $(-x+1/2, -y+1/2, -z)$. These characteristics indicate that $YbMnSb_2$ has $IT(1/2, 1/2)$ symmetry (I represents the spatial inversion, and T represents time reversal), which restricts the Berry curvature to zero in the whole first Brillouin zone and that the intrinsic ANE is not expected to exist in this system [51,52]. Furthermore, the magnetization of $YbMnSb_2$ with the $B \parallel c$ configuration increases smoothly with increasing field, reaches a maximum of about 0.1 emu/g at 2.2 K and 14 T [31]. The so tiny magnetization together with the smooth magnetic-field dependence, indicates that there is no field-induced metamagnetic transition in this system, revealing that $YbMnSb_2$ keeps the same AFM ordering state and, thus, the same gapped Dirac state under the external field up to 14 T. In addition, the Nernst signal at around 120 K increases with the increasing temperature and reaches a maximum of about 40 $\mu V\,K^{-1}$ at 14 T with no sign of saturation, which is quite different from the behavior of usual ANE. Thus, the large Nernst signal in $YbMnSb_2$ is not likely to stem from the intrinsic Berry curvature. As discussed in the Seebeck and Hall measurements, the hole-type carrier dominates the transport properties. Thus, we simplified $YbMnSb_2$ as a single band system and discussed its large Nernst effect according to classical theory. Usually, $\sigma_{xx} \gg \sigma_{xy}$, and the Nernst signal can be written as [47]

$$S_{xy} = \frac{\pi^2}{3}\frac{k_B^2 T}{e}\frac{\partial \tan\theta_H}{\partial \varepsilon}\bigg|_{\varepsilon=\varepsilon_F} = \frac{\pi^2}{3}\frac{k_B^2 T}{e}\frac{\mu B}{\varepsilon_F}, \qquad (4)$$

where $\tan\theta_H = \sigma_{xy}/\sigma_{xx}$ is the Hall angle. $\tan\theta_H/B = \frac{e\tau}{m^*} = \mu$, τ represents the relaxation time, m^* and μ are the effective mass and mobility, respectively. As discussed in the transport measurements and analysis, $YbMnSb_2$ exhibits high mobility. According to the first-principles calculations and quantum oscillations, the Fermi energy of this system is very small. Thus, we conclude that the large Nernst effect in $YbMnSb_2$ could mainly result from the high mobility and small ε_F. The phonon drag effect caused by the electron-phonon interaction could also enlarge both the Nernst effect and the thermopower [42,53,54]. Figure 4(c) presents the temperature-dependent Nernst coefficient divided by temperature (v/T) at 14 T and the thermopower divided by temperature (S_{xx}/T) at zero field, both of which show a broad dip around 60 K. It should be noted that v/T and S_{xx}/T display the opposite sign, indicating that the Nernst coefficient is enhanced, whereas, the thermopower is weakened around 60 K. Thus, the large Nernst effect in $YbMnSb_2$ is not caused by the phonon drag effect. In addition, the broad peaks around 60 K in v/T and S_{xx}/T are also an indication of the possible temperature-induced Lifshitz transition, which is consistent with the results of the Hall measurements and the calculations.

IV. CONCLUSION

In conclusion, we observed quantum oscillations in the MS effect, and several frequencies are extracted after FFT analysis. After fitting by the thermal damping factor, the effective mass $\sim 0.07 m_e$ of the major frequency is obtained, which probably stems from the highly dispersive Dirac bands according to the first-principles calculations. The large Nernst effect was observed, which reaches the maximum around 120 K, and the corresponding Nernst thermopower of about 40 $\mu V\,K^{-1}$ at 14 T is achieved. Combining the analysis of the quantum oscillations, the Hall effect and the first-principles calculations, we attribute the large Nernst effect to the high mobility and small ε_F. A possible moderate temperature-induced Lifshitz transition around 60 K is also revealed by the electric, thermoelectric measurements, and the first-principles calculations from which the modified carrier properties could further enhance the Nernst signal through the so-called ambipolar effect. Our work further indicates that the large Nernst effect could be a universal feature in such topological semimetals in which the high mobility and small ε_F are their typical characteristics due to the topological protected band structures.

ACKNOWLEDGMENTS

This work was supported by The National Key Projects for Research & Development of China (Grant No. 2019YFA0308602), the National Natural Science Foundation of China (Grants No. 12174334 and No. 12204410), the Innovation program for Quantum Science and Technology (Grant No. 2021ZD0302500), and China Postdoctoral Science Foundation (Grant No. 2022M712788)

[1] H. Zhang, C.-X. Liu, X.-L. Qi, X. Dai, Z. Fang, and S.-C. Zhang, Nat. Phys. **5**, 438 (2009).
[2] X. Wan, A. M. Turner, A. Vishwanath, and S. Y. Savrasov, Phys. Rev. B **83**, 205101 (2011).
[3] A. A. Burkov, M. D. Hook, and L. Balents, Phys. Rev. B **84**, 235126 (2011).
[4] Z. Wang, Y. Sun, X.-Q. Chen, C. Franchini, G. Xu, H. Weng, X. Dai, and Z. Fang, Phys. Rev. B **85**, 195320 (2012).
[5] K. Biswas, J. He, I. D. Blum, C.-I. Wu, T. P. Hogan, D. N. Seidman, V. P. Dravid, and M. G. Kanatzidis, Nature (London) **489**, 414 (2012).
[6] L.-D. Zhao, S.-H. Lo, Y. Zhang, H. Sun, G. Tan, C. Uher, C. Wolverton, V. P. Dravid, and M. G. Kanatzidis, Nature (London) **508**, 373 (2014).
[7] J. P. Heremans, R. J. Cava, and N. Samarth, Nat. Rev. Mater. **2**, 17049 (2017).

[8] J. He and T. M. Tritt, Science **357**, eaak9997 (2017).
[9] J. Mao, H. Zhu, Z. Ding, Z. Liu, G. A. Gamage, G. Chen, and Z. Ren, Science **365**, 495 (2019).
[10] K. Behnia and H. Aubin, Rep. Prog. Phys. **79**, 046502 (2016).
[11] K. Behnia, J. Phys.: Condens. Matter **21**, 113101 (2009).
[12] S. J. Watzman, T. M. McCormick, C. Shekhar, S.-C. Wu, Y. Sun, A. Prakash, C. Felser, N. Trivedi, and J. P. Heremans, Phys. Rev. B **97**, 161404(R) (2018).
[13] A. Sakai, S. Minami, T. Koretsune, T. Chen, T. Higo, Y. Wang, T. Nomoto, M. Hirayama, S. Miwa, D. Nishio-Hamane *et al.*, Nature (London) **581**, 53 (2020).
[14] R. Bel, K. Behnia, and H. Berger, Phys. Rev. Lett. **91**, 066602 (2003).
[15] T. Liang, J. Lin, Q. Gibson, T. Gao, M. Hirschberger, M. Liu, R. J. Cava, and N. P. Ong, Phys. Rev. Lett. **118**, 136601 (2017).
[16] J. Xiang, S. Hu, M. Lyu, W. Zhu, C. Ma, Z. Chen, F. Steglich, G. Chen, and P. Sun, Sci. China Phys. Mech. Astron. **63**, 237011 (2020).
[17] F. Caglieris, C. Wuttke, S. Sykora, V. Süss, C. Shekhar, C. Felser, B. Büchner, and C. Hess, Phys. Rev. B **98**, 201107(R) (2018).
[18] M. Ikhlas, T. Tomita, T. Koretsune, M.-T. Suzuki, D. Nishio-Hamane, R. Arita, Y. Otani, and S. Nakatsuji, Nat. Phys. **13**, 1085 (2017).
[19] L. Ding, J. Koo, L. Xu, X. Li, X. Lu, L. Zhao, Q. Wang, Q. Yin, H. Lei, B. Yan *et al.*, Phys. Rev. X **9**, 041061 (2019).
[20] S. N. Guin, P. Vir, Y. Zhang, N. Kumar, S. J. Watzman, C. Fu, E. Liu, K. Manna, W. Schnelle, J. Gooth *et al.*, Adv. Mater. **31**, 1806622 (2019).
[21] A. Sakai, Y. P. Mizuta, A. A. Nugroho, R. Sihombing, T. Koretsune, M.-T. Suzuki, N. Takemori, R. Ishii, D. Nishio-Hamane, R. Arita *et al.*, Nat. Phys. **14**, 1119 (2018).
[22] S. N. Guin, Q. Xu, N. Kumar, H. Kung, S. Dufresne, C. Le, P. Vir, M. Michiardi, T. Pedersen, S. Gorovikov, S. Zhdanovich, K. Manna, G. Auffermann, W. Schnelle, J. Gooth, C. Shekhar, A. Damascelli, Y. Sun, and C. Felser, Adv. Mater. **33**, 2006301 (2021).
[23] C. Liu, T. Kondo, R. M. Fernandes, A. D. Palczewski, E. D. Mun, N. Ni, A. N. Thaler, A. Bostwick, E. Rotenberg, J. Schmalian *et al.*, Nat. Phys. **6**, 419 (2010).
[24] C. Liu, A. D. Palczewski, R. S. Dhaka, T. Kondo, R. M. Fernandes, E. D. Mun, H. Hodovanets, A. N. Thaler, J. Schmalian, S. L. Budko *et al.*, Phys. Rev. B **84**, 020509(R) (2011).
[25] S. L. Bud'ko, A. N. Voronovskii, A. G. Gapotchenko, and E. S. Itskevich, Zh. Eksp. Teor. Fiz. **86**, 778 (1984) [Sov. Phys. JETP **59**, 454 (1984)].
[26] D. Kang, Y. Zhou, W. Yi, C. Yang, J. Guo, Y. Shi, S. Zhang, Z. Wang, C. Zhang, S. Jiang, A. Li, K. Yang, Q. Wu, G. Zhang, L. Sun, and Z. Zhao, Nat. Commun. **6**, 7804 (2015).
[27] G. Chen, *Nanoscale Energy Transport and Conversion: A Parallel Treatment of Electrons, Molecules, Phonons, and Photons* (Oxford University Press, Oxford, 2005).
[28] Y. Wu, N. H. Jo, M. Ochi, L. Huang, D. Mou, S. L. Budko, P. C. Canfield, N. Trivedi, R. Arita, and A. Kaminski, Phys. Rev. Lett. **115**, 166602 (2015).
[29] Y. Zhang, C. Wang, L. Yu, G. Liu, A. Liang, J. Huang, S. Nie, X. Sun, Y. Zhang, B. Shen *et al.*, Nat. Commun. **8**, 15512 (2017).
[30] J. Wang, H. Yang, L. Ding, W. You, C. Xi, J. Cheng, Z. Shi, C. Cao, Y. Luo, Z. Zhu *et al.*, npj Quantum Mater. **4**, 58 (2019).
[31] Y.-Y. Wang, S. Xu, L.-L. Sun, and T.-L. Xia, Phys. Rev. Mater. **2**, 021201(R) (2018).
[32] R. Kealhofer, S. Jang, S. M. Griffin, C. John, K. A. Benavides, S. Doyle, T. Helm, P. J. W. Moll, J. B. Neaton, J. Y. Chan *et al.*, Phys. Rev. B **97**, 045109 (2018).
[33] Z. Qiu, C. Le, Z. Liao, B. Xu, R. Yang, J. Hu, Y. Dai, and X. Qiu, Phys. Rev. B **100**, 125136 (2019).
[34] J.-R. Soh, S. M. Tobin, H. Su, I. Zivkovic, B. Ouladdiaf, A. Stunault, J. A. Rodriguez-Velamazan, K. Beauvois, Y. Guo, and A. T. Boothroyd, Phys. Rev. B **104**, L161103 (2021).
[35] A. A. Mostofi, J. R. Yates, G. Pizzi, Y.-S. Lee, I. Souza, D. Vanderbilt, and N. Marzari, Comput. Phys. Commun. **185**, 2309 (2014).
[36] Y. Pan, F.-R. Fan, X. Hong, B. He, C. Le, W. Schnelle, Y. He, K. Imasato, H. Borrmann, C. Hess *et al.*, Adv. Mater. **33**, 2003168 (2021).
[37] D. Shoenberg, *Magnetic Oscillations in Metals* (Cambridge University Press, Cambridge, UK, 2009).
[38] R. Fletcher, J. Low Temp. Phys. **43**, 363 (1981).
[39] R. Fletcher, Phys. Rev. B **28**, 1721 (1983).
[40] B. Tieke, R. Fletcher, J. C. Maan, W. Dobrowolski, A. Mycielski, and A. Wittlin, Phys. Rev. B **54**, 10565 (1996).
[41] A. Palacio Morales, A. Pourret, G. Knebel, G. Bastien, V. Taufour, D. Aoki, H. Yamagami, and J. Flouquet, Phys. Rev. B **93**, 155120 (2016).
[42] X. Xu, X. Wang, T. A. Cochran, D. S. Sanchez, G. Chang, I. Belopolski, G. Wang, Y. Liu, H.-J. Tien, X. Gui *et al.*, Phys. Rev. B **100**, 045104 (2019).
[43] R. Young, J. Phys. F: Met. Phys. **3**, 721 (1973).
[44] See Supplemental Material at http://link.aps.org/supplemental/10.1103/PhysRevB.107.245138 for the figures of the XRD pattern, the EDS map of the single crystal, and the simplified dispersion map of the nodal line.
[45] Y. Gan, W. Xia, L. Zhang, K. Yang, X. Mi, A. Wang, Y. Chai, Y. Guo, X. Zhou, and M. He, Phys. Rev. B **104**, L180508 (2021).
[46] R. Bel, K. Behnia, Y. Nakajima, K. Izawa, Y. Matsuda, H. Shishido, R. Settai, and Y. Onuki, Phys. Rev. Lett. **92**, 217002 (2004).
[47] Y. Wang, Z. A. Xu, T. Kakeshita, S. Uchida, S. Ono, Y. Ando, and N. P. Ong, Phys. Rev. B **64**, 224519 (2001).
[48] X. Zhou, H. Liu, W. Wu, K. Jiang, Y. Shi, Z. Li, Y. Sui, J. Hu, and J. Luo, Phys. Rev. B **105**, 205104 (2022).
[49] S. Borisenko, D. Evtushinsky, Q. Gibson, A. Yaresko, K. Koepernik, T. Kim, M. Ali, J. v. d. Brink, M. Hoesch, A. Fedorov, E. Haubold, Y. Kushnirenko, I. Soldatov, R. Schäfer, and R. J. Cava, Nat. Commun. **10**, 3424 (2019).
[50] Y. Pan, C. Le, B. He, S. J. Watzman, M. Yao, J. Gooth, J. P. Heremans, Y. Sun, and C. Felser, Nature Mater. **21**, 203 (2022).
[51] L. Šmejkal, A. H. MacDonald, J. Sinova, S. Nakatsuji, and T. Jungwirth, Nat. Rev. Mater. **7**, 482 (2022).
[52] P.-J. Guo, Z.-X. Liu, and Z.-Y. Lu, npj Comput. Mater. **9**, 70 (2023)
[53] S. Lyo, Phys. Rev. B **17**, 2545 (1978).
[54] R. D. Barnard and V. Cannella, Phys. Today **27**(9), 52 (1974).